EAI Endorsed Transactions
on Energy Web
Research Article EAI.EU

Transient Characteristics and Transient Power Angle Stability Analysis of Synchronous Condenser Considering the Influence of Different Renewable Energy Active Outputs

Cheng Lü[1], Taitian Sun[2], Xingwei Xu[3], Yafei Zhang[4], Yibo Zhou[2,*], Yuanfei Lin[2]

[1] China General Nuclear Corporation (Ulanqab) Wind Power Co., Ltd., Ulanqab 013550, China
[2] Key Laboratory of Modern Power System Simulation and Control & Renewable Energy Technology, Ministry of Education (Northeast Electric Power University), Jilin 132012, China
[3] Northeast Branch of State Grid Corporation of China, Shenyang 110180, China
[4] China General Nuclear Corporation (Xing'an League) New Energy Co., Ltd., Xing'an League 137700, China

Abstract

INTRODUCTION: Synchronous condensers (SCs) are installed near renewable energy stations to suppress transient overvoltage and enhance transmission capacity, but they increase SC transient power-angle instability risk post-fault.
OBJECTIVES: To analyze the transient instability mechanism of SC, the transient characteristics during and after faults, and the influence law of different renewable energy active power outputs on SC transient power-angle stability.
METHODS: First, a transient stability analysis model of SC is established. Second, based on the equal-area criterion, the mechanism of SC transient power-angle instability is analyzed, followed by an analysis of the SC's transient characteristics. Finally, combined with the trajectory analysis method, the influence mechanism of different renewable energy active power outputs on SC transient power-angle stability is revealed from the perspective of stability indices.
RESULTS: By building a simplified simulation model of the renewable energy transmission system in PSASP, the transient parameter results and stability indices of SC under different operating conditions are obtained, which verifies the correctness of the mechanism analysis in this paper.
CONCLUSION: Fault-induced reverse active power absorption accelerates SC rotors and triggers transient instability, and higher renewable energy output intensifies SC power-angle swing, aggravates voltage drop and reduces stability index.

Keywords: synchronous condenser, transient power-angle stability, renewable energy active output, transient characteristics.

Received on 15 January 2026, accepted on 31 March 2026, published on 05 May 2026

doi: 10.4108/ew.11586

1. Introduction

With the formal and comprehensive implementation of the "dual-carbon" target, the integration scale of renewable energy in terms of installed capacity and electricity generation has maintained a stable and continuous annual upward trend [1]. As of the end of July 2025, the installed capacity of solar power had reached 1.11 billion kilowatts, which stands for a year-on-year increase of 50.8%, while the installed capacity of wind power was recorded at 570 million kilowatts, with a year-on-year growth rate of 22.1% [2]. The development of a new power system that is

*Corresponding author. Email: zhouyiboaa@126.com

featured by an increasingly high proportion of renewable energy is therefore progressing at an accelerated and steady pace [3]. However, in the specific context of long-distance power transmission from large-scale renewable energy bases, key technical issues such as transient overvoltage [4-5] and wide-band oscillation have become increasingly prominent, and this situation poses significant risks of involuntary disconnection and operational withdrawal of renewable energy units [6]. To effectively address the challenge of transient overvoltage, distributed synchronous condensers (SCs) which serve as reliable dynamic reactive power compensation devices have been widely deployed in the immediate vicinity of renewable energy stations [7-8], and this deployment has effectively enhanced the overall stability of the power system and the voltage support capability of renewable energy sources [9]. Nevertheless, massive-scale power grid integration of renewable energy has drastically and significantly changed the original distribution pattern of system power flow [10]. As typical synchronous rotating machines, the synchronization mechanism of these SCs is still primarily governed by the rotor motion equation, and this characteristic renders them highly vulnerable to transient power-angle instability under the influence of unbalanced power when a short-circuit disturbance takes place in the power system [11-12].

Distributed SCs which are characterized by small individual capacity and low rotational inertia are typically deployed in close proximity to renewable energy stations, and this deployment pattern makes them highly susceptible to the inherent fluctuations in renewable energy output. Regarding the in-depth analysis of the transient power-angle stability of such SCs, existing research work has achieved notable and certain progress. Shen et al. systematically performed Norton equivalence analysis on renewable energy bases that incorporate SCs, successfully established and proposed a practical capacity conversion method between renewable energy sources and equivalent synchronous units, and comprehensively assessed the transient stability of the SCs from the dedicated standpoint of the critical short-circuit ratio [13]. Li et al. models the active generation of renewable energy as a current that is injected into the condenser and the receiving-end synchronous machine; by making use of the equal-area rule, it thoroughly elucidates the instability mechanisms induced by different types of faults and low penetration depths, and at the same time proposes a clear transient instability criterion [14]. Wang et al. carefully carried out a detailed qualitative analysis through the phase method, focusing on investigating the interaction mechanism between the SC's power angle and the voltage at the point of common coupling (PCC) for renewable energy after the clearance of faults, as well as the specific impacts of transition resistors and renewable energy low voltage ride-through (LVRT) control strategies on the transient oscillation process of the SCs [15]. Wang et al. thoroughly clarifies the underlying and intrinsic mechanism through which the key control parameters of inverter-based power supply LVRT and its recovery process influence the transient stability of SCs [16]. Liu et al. effectively applied the superposition theorem to equate the integrated system to a single synchronous machine, revealed the transient instability mechanism of the SCs through the unbalanced power that is borne by the rotor, and assessed the transient stability margin of the SCs using the Lyapunov direct method [17]. For high-resistance faults, Liu et al. carefully derived the power-angle characteristic equation for this specific operating condition to uncover the intrinsic and fundamental instability mechanisms of SCs, and constructed specific quantitative indices based on critical clearing time to thoroughly explore the influence laws of system parameters on transient stability [18]. Building on the theoretical model established in Li et al., Zhao et al. fully made use of the equal-area rule to analyze the specific effects of key influencing factors including electrical distance, the inertia of SCs, and renewable energy control strategies on the transient stability of the SCs [19].

However, existing research studies still suffer from notable and obvious operational limitations: they predominantly focus on specific scenarios in which the transient characteristics of the SCs are dominated by system failure parameters or renewable energy control strategies. The transient instability mechanism of the SCs is only qualitatively analyzed through the equal-area rule, failing to comprehensively depict the transient instability morphology by integrating the power-angle characteristics obtained from the derivation of the specific model and the actual specific system parameters. Current research focusing on how renewable energy active power output influences the transient stability characteristics of SCs lacks in-depth mechanistic interpretation.

To resolve the above-mentioned problems, this paper focuses on investigating the transient characteristics and transient power-angle stability performance of SCs considering the impacts of different active power outputs of renewable energy units. First, based on the equivalent circuit obtained through system simplification, an analytical theoretical model for the transient power-angle stability of SC is established. Analytical expressions of the power-angle characteristic coupled with active power generation of variable renewable energy are derived for the steady-state operation, fault period and post-fault clearing stages. Second, specific system parameters are set. The transient instability mode of the SC is revealed based on the equal-area criterion. Meanwhile, the transient characteristics of the SC under different active power outputs of renewable energy sources are analyzed according to the analytical formulations describing PCC voltage and electromagnetic power at the PCC for renewable energy during and after the fault. Finally, based on the trajectory analysis method [20], the influence mechanism of different active power levels of renewable energy on the stability index is discussed, leading to the conclusion that an increase in the active power delivery of renewable energy sources exerts a negative impact on the stability index. A simplified renewable energy transmission system with the SC is built in PSASP. The transient stability of the SC is quantitatively evaluated

using the stability index, which confirms the validity of the aforementioned theoretical derivation.

2. Analysis model for transient power-angle stability of SC

To facilitate the analysis of the SC's transient power-angle stability effectively, this paper constructs a renewable energy power transmission system through AC transmission lines, and the particular configuration of this system is depicted in Figure 1. (a). This system is specifically configured with a SC at the PCC.

The topology of the renewable energy transmission system containing SC is clearly shown in Figure 1. (b), and each parameter in this topology is defined in detail as follows: X_{sc} represents the superposition of the transient reactance X_d' of the synchronous condenser and the transformer reactance X_T ; X_w corresponds to the reactance of the renewable energy step-up transformer; X_L stands for the equivalent reactance of the transmission line and the associated transformer; E_s specifically denotes the magnitude of the internal potential of the equivalent synchronous machine in the receiving system, with its rotor angle set to 0° and used as the reference angle; the transient electromagnetic potential of the synchronous condenser is $\dot{E}'$, whose voltage magnitude is E' and phase angle is δ_{sc} ; bus b is the PCC where the renewable energy source and the synchronous condenser are jointly connected for power transmission, with its voltage amplitude being U_b and voltage phase angle relative to the reference angle being δ_b . P_{sc} and Q_{sc} are the active power and reactive power supplied by the SC, in that order; P_w and Q_w are the active power and reactive power actually generated by the renewable energy source, in that order; P_s and Q_s correspond to the active power and reactive power transmitted via the receiving-end power grid.

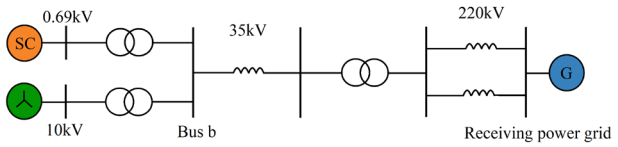

(a) System structure diagram

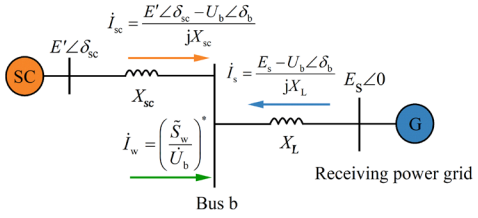

(b) System topology diagram

Figure 1. The equivalent representation of the simplified renewable energy power transmission scheme incorporating SC

In order to effectively facilitate further in-depth mechanistic analysis, the following specific simplified assumptions are put forward for the dynamic model of the system: (1) SC adopts the classical second-order model of synchronous machines, and it is assumed that SC can achieve rapid excitation to maintain the constant value of its terminal voltage; (2) Based on the time scale of electromechanical transients, the dynamic change process of the current inner loop of renewable energy converters is not taken into account [21]. When a fault occurs at the remote end, it is assumed by default that the active power delivered by renewable energy sources fluctuates slightly during the fault period and after fault clearance, basically remaining at the steady-state level, and renewable energy sources adopt the constant power model; (3) The series line resistance in the system is neglected, and a large-capacity and high-inertia synchronous machine is used to simulate the receiving-end system; (4) Considering that the reactance value of renewable energy step-up transformers is relatively small, the power loss of the output power at the renewable energy machine terminals before it flows into bus b is neglected.

The basic rotor motion dynamics of the SC can be described by the following expressions:

$$\begin{cases} \dfrac{\mathrm{d}\delta_{sc}}{\mathrm{d}t}=\omega_N\cdot\omega_{sc} \\ \dfrac{\mathrm{d}\omega_{sc}}{\mathrm{d}t}=\dfrac{1}{T_j}\left(P_T-P_{sc}\right) \end{cases} \tag{1}$$

ω_{sc} is defined as the angular velocity of the SC, and ω_N represents the power system's rated angular velocity; T_j denotes the SC rotor's inertia time constant; P_T denotes the mechanical power of the SC, and since the SC has no prime mover, it is approximated as zero; P_{sc} refers to the SC's electromagnetic power; the damping effect of the SC is not taken into account, so the damping coefficient D is set to zero.

Based on the aforementioned assumptions, this paper will analyze the SC's transient power-angle stability from the perspective of simplifying the power system into an equivalent circuit by deriving relevant analytical expressions. The equivalent current $\dot{I}_{sc}$ of the SC and the equivalent current $\dot{I}_s$ of the infinite bus system at the receiving end are shown in Figure 2. (a), and they satisfy the following specific relationships:

$$\dot{I}_{sc}=\frac{E'\angle\delta_{sc}-U_b\angle\delta_b}{jX_{sc}} \tag{2}$$

$$\dot{I}_s=\frac{E_s-U_b\angle\delta_b}{jX_L} \tag{3}$$

The equivalent current of renewable energy sources is represented by the $\left(\tilde{S}_w/\dot{U}_b\right)^*$ derived from the principle of power conservation:

$$\dot{I}_{\mathrm{w}}=\left(\frac{\tilde{S}_{\mathrm{w}}}{\dot{U}_{\mathrm{b}}}\right)^{*}=\frac{P_{\mathrm{w}}-\mathrm{j}Q_{\mathrm{w}}}{U_{\mathrm{b}}\angle-\delta_{\mathrm{b}}}=\frac{(P_{\mathrm{w}}-\mathrm{j}Q_{\mathrm{w}})\cdot(\cos\delta_{\mathrm{b}}+\mathrm{j}\sin\delta_{\mathrm{b}})}{U_{\mathrm{b}}} \quad (4)$$

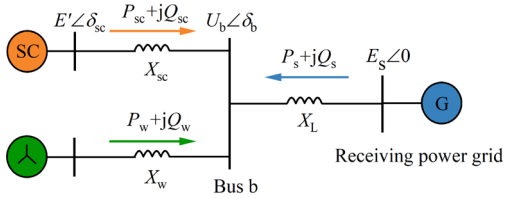

(a) Simplified system topology diagram

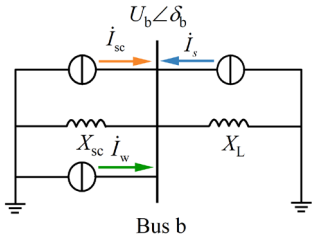

(b) Simplified system equivalent circuit diagram

Figure 2. Model of the renewable energy electric power transmission system incorporating SC

Three equivalent current sources are injected into bus b simultaneously, and the voltage at bus b can be derived from the equivalent circuit shown in Figure 2. (b):

$$\dot{U}_{\mathrm{b}}=\mathrm{j}\frac{X_{\mathrm{sc}}\cdot X_{\mathrm{L}}}{X_{\mathrm{sc}}+X_{\mathrm{L}}}\cdot\left(\dot{I}_{\mathrm{sc}}+\dot{I}_{\mathrm{s}}+\dot{I}_{\mathrm{w}}\right) \quad (5)$$

Let $X_{\mathrm{I}}=\left(X_{\mathrm{sc}}\cdot X_{\mathrm{L}}\right)/\left(X_{\mathrm{sc}}+X_{\mathrm{L}}\right)$, and substituting Equations (2), (3) and (4) into Equation (5) to expand and simplify:

$$\begin{cases}A\cos\delta_b+B\sin\delta_b=C\\-B\cos\delta_b+A\sin\delta_b=D\end{cases} \quad (6)$$

Where $A=2U_{\mathrm{b}}-Q_{\mathrm{w}}X_{\mathrm{I}}/U_{\mathrm{b}}$, $B=P_{\mathrm{w}}X_{\mathrm{I}}/U_{\mathrm{b}}$, $C=E'X_{\mathrm{I}}\cos\delta_{\mathrm{sc}}/X_{\mathrm{sc}}+E_{\mathrm{s}}X_{\mathrm{I}}/X_{\mathrm{L}}$, $D=E'X_{\mathrm{I}}\sin\delta_{\mathrm{sc}}/X_{\mathrm{sc}}$.

Solving the coefficient determinant matrix yields:

$$\begin{cases}\sin\delta_b=\dfrac{BC+AD}{\Delta}\\\cos\delta_b=\dfrac{AC-BD}{\Delta}\end{cases} \quad (7)$$

Where $\Delta=\left(2U_{\mathrm{b}}-Q_{\mathrm{w}}X_{\mathrm{I}}/U_{\mathrm{b}}\right)^2+\left(P_{\mathrm{w}}X_{\mathrm{I}}/U_{\mathrm{b}}\right)^2$, the detailed expressions for $\sin\delta_{\mathrm{b}}$, $\cos\delta_{\mathrm{b}}$ are shown in Equation (7) in Appendix A.

Square both sides of the two Equations in Equation (6) respectively, then add them correspondingly. Based on the voltage distribution of the simplified renewable energy transmission system, it follows that:

$$4U_{\mathrm{b}}^2-\left(4Q_{\mathrm{w}}X_{\mathrm{I}}+\frac{E'^2X_{\mathrm{I}}^2}{X_{\mathrm{sc}}^2}+\frac{2E'E_{\mathrm{s}}X_{\mathrm{I}}^2\cos\delta_{\mathrm{sc}}}{X_{\mathrm{sc}}X_{\mathrm{L}}}+\frac{E_{\mathrm{s}}^2X_{\mathrm{I}}^2}{X_{\mathrm{L}}^2}\right)U_{\mathrm{b}}^2+P_{\mathrm{w}}^2X_{\mathrm{I}}^2+Q_{\mathrm{w}}^2X_{\mathrm{I}}^2=0 \quad (8)$$

Let $E=4Q_{\mathrm{w}}X_{\mathrm{I}}+E'^2X_{\mathrm{I}}^2/X_{\mathrm{sc}}^2+2E'E_{\mathrm{s}}X_{\mathrm{I}}^2\cos\delta_{\mathrm{sc}}/X_{\mathrm{sc}}X_{\mathrm{L}}+E_{\mathrm{s}}X_{\mathrm{I}}^2/X_{\mathrm{L}}^2$, $F=P_{\mathrm{w}}^2X_{\mathrm{I}}^2+Q_{\mathrm{w}}^2X_{\mathrm{I}}^2$. The expression for the voltage amplitude at the renewable energy grid connection bus b can be derived as:

$$U_{\mathrm{b}}=\sqrt{\frac{E+\sqrt{E^2-16F}}{8}} \quad (9)$$

The expression for U_{b} is provided in Equation (9) in Appendix A.

Based on the output power of the SC, it follows that:

$$P_{\mathrm{sc}}=\frac{E'U_{\mathrm{b}}}{X_{\mathrm{sc}}}\sin\left(\delta_{\mathrm{sc}}-\delta_{\mathrm{b}}\right) \quad (10)$$

Substituting Equations (7) and (9) into Equation (10), the expression for the electromagnetic power of the SC under steady-state operation, considering the impact of variations in the active power outputs from renewable energy units, is obtained:

$$P_{\mathrm{sc1}}=\frac{E'}{X_{\mathrm{sc}}}\cdot\frac{U_{\mathrm{b}}^2\cdot\left[\left(2U_{\mathrm{b}}^2-Q_{\mathrm{w}}X_{\mathrm{I}}\right)\frac{E_{\mathrm{s}}X_{\mathrm{I}}\sin\delta_{\mathrm{sc}}}{X_{\mathrm{L}}}-P_{\mathrm{w}}X_{\mathrm{I}}\left(\frac{E'X_{\mathrm{I}}}{X_{\mathrm{sc}}}+\frac{E_{\mathrm{s}}X_{\mathrm{I}}\cos\delta_{\mathrm{sc}}}{X_{\mathrm{L}}}\right)\right]}{\left(2U_{\mathrm{b}}^2-Q_{\mathrm{w}}X_{\mathrm{I}}\right)^2+\left(P_{\mathrm{w}}X_{\mathrm{I}}\right)^2} \quad (11)$$

This expression also incorporates the effect of the PCC voltage for renewable energy on the SC's electromagnetic power. Unlike the typical single-machine infinite-bus (SMIB) system, the active and reactive power outputs of renewable energy are integrated into the SC's electromagnetic power, thereby influencing its power-angle characteristics. To facilitate analyzing the impact of renewable energy's active power output on the SC and eliminate the interference of reactive power, it is assumed that under steady-state operation, the renewable energy operates with constant power factor control—i.e., only active power is injected, while no reactive power is supplied.

The system parameters are set as follows: $E'=1.2$, $E_{\mathrm{s}}=1.0$, $X_{\mathrm{sc}}=0.2593$, $X_{\mathrm{L}}=0.260$, $X_{\mathrm{I}}=0.1298$ all in per unit (p.u.) values, with a system base capacity of 100 MVA. Under the premise of a given SC capacity and $Q_{\mathrm{w}}=0$, with the rated active power output of renewable energy as the operating condition, the power-angle characteristic curve of the SC, as shown in Figure 3, can be plotted based on Equation (11).

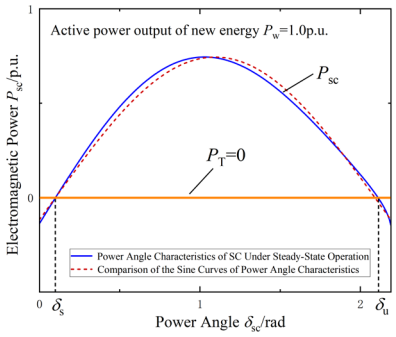

Figure 3. The power-angle characteristic curve for the SC in steady-state operation

From Figure 3, it can be observed that the SC installed in the renewable energy power plant alters the sinusoidal shape of the power-angle characteristic curve, which is no longer a symmetric sine wave. This demonstrates that the connection of renewable energy to the power grid has modified the power transmission relationship of the SC, resulting in a more complex nonlinear relationship between the SC's electromagnetic power and rotor angle.

3. Analysis of the transient instability mechanism of the SC during fault periods

This paper adopts the most extreme case of three-phase metallic short-circuit fault as a representative example and explores the mechanism of the SC's transient power-angle instability during fault periods by virtue of the equal area criterion. If a fault takes place near the PCC, the SC's electromagnetic power becomes zero, so $P_T - P_{sc}$ equals zero and there is no accelerating power to trigger SC's transient power-angle instability. When the fault occurs at the remote end, due to the weak disturbance characteristic of remote faults, variations in LVRT strategies for renewable energy units, as well as the synergistic effect of optimal dispatch, the actual active power delivery of these units maintains a basically stable state throughout the fault period, without any significant reduction. The equivalent circuit when the fault occurs at the farthest end is presented in Figure 4, and the expression corresponding to P_{sc2}, the electromagnetic power of the SC during fault occurrence, is as follows:

$$P_{sc2} = -\frac{E'^2 U_b^{\,2} X_1^{\,2} P_w}{X_{sc}^{\,2}\left[\left(U_b^{\,2}\cdot\frac{X_{sc}+X_1}{X_{sc}} - Q_w X_1\right)^2 + (P_w X_1)^2\right]} \tag{12}$$

The square of the voltage amplitude at the PCC during the fault period is as follows:

$$U_b''^2 = \frac{2Q_w X_1 X_{sc}(X_{sc}+X_1) + E'^2 X_1^{\,2} + \sqrt{\Delta'}}{2(X_{sc}+X_1)^2} \tag{13}$$

Among them, $\Delta' = \left[2Q_w X_1 X_{sc}(X_{sc}+X_1) + E'^2 X_1^{\,2}\right]^2 - 4X_{sc}^{\,2}(X_{sc}+X_1)^2\cdot(Q_w^{\,2} X_1^{\,2} + P_w^{\,2} X_1^{\,2})$.

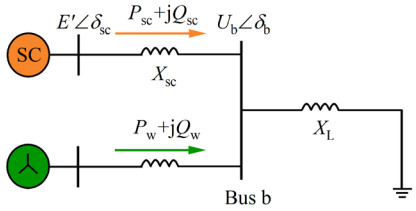

(a) The topology diagram of the system

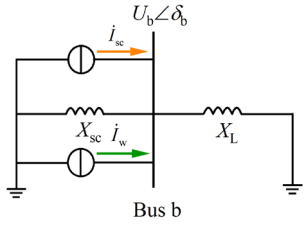

(b) The equivalent circuit diagram

Figure 4. The simplified renewable energy power transmission system during the fault period

Based on the basic relationships between renewable energy sources and the SC in Figure 4, combined with Equations (12) and (13), it can be derived that $P_{sc} + P_w = 0$. That is to say, during the electromechanical transient process, the sum of the electromagnetic power of the SC and the active power delivery of renewable energy units is zero during remote three-phase metallic short-circuit faults. This indicates that the active power delivery of renewable energy units is fed back to the SC during the fault period, leading to the acceleration of its rotor and thus increasing the risk of the SC's transient power-angle instability.

After fault clearing, the voltage amplitude at the PCC and the SC's electromagnetic power can be calculated by the method analogous to that in the steady state before the fault. Since X_L is changed after fault clearing and the system reactance becomes $X_L' = 0.323$, X_1 is changed to $X_1' = 0.1438$. Thus, the PCC voltage amplitude is changed to U_b', with the detailed expression provided in Equation (24) in Appendix A.

The expression for P_{sc3} can be expressed as:

$$P_{sc3} = \frac{E'}{X_{sc}}\cdot\frac{U_b'^2\cdot\left[\left(2U_b'^2 - Q_w X_1'\right)\frac{E_x X_1'\sin\delta_{sc}}{X_L'} - P_w X_1'\left(\frac{E'X_1'}{X_{sc}} + \frac{E_x X_1'\cos\delta_{sc}}{X_L'}\right)\right]}{(2U_b'^2 - Q_w X_1')^2 + (P_w X_1')^2} \tag{14}$$

The change in the voltage amplitude at the PCC caused by the system reactance indirectly leads to the shift of the SC's power-angle characteristic curve after the fault.

Assume a remote three-phase metallic short-circuit fault, with its initiation time at t_1 and clearance time at t_2. Combined with Equation (1), the corresponding power angle at the fault clearing time can be derived as δ_c:

$$\delta_c = \delta_0 + \frac{1}{2}\omega_N \frac{P_T - P_{sc2}}{T_j}(t_2 - t_1)^2 \tag{15}$$

By combining $P_T = 0$ with Equation (11), the δ_s corresponding to the stable equilibrium point can be obtained. Similarly, by combining $P_T = 0$ with Equation (14), the δ_u corresponding to the unstable equilibrium point can be obtained, and the accelerating area of the SC is as follows:

$$S_1 = (P_T - P_{sc2})\cdot(\delta_c - \delta_0) \tag{16}$$

The maximum decelerating area is as follows:

$$S_{2\max}=\int_{\delta_c}^{\delta_u}\frac{E'}{X_{sc}}\cdot\frac{U_b'^2\left[\left(2U_b'^2-Q_wX_l'\right)\frac{E_sX_l'\sin\delta_{sc}}{X_L'}-P_wX_l'\left(\frac{E'X_l'}{X_{sc}}+\frac{E_sX_l'\cos\delta_{sc}}{X_L'}\right)\right]}{\left(2U_b'^2-Q_wX_l'\right)^2+\left(P_wX_l'\right)^2}d\delta_{sc} \quad (17)$$

Based on the aforementioned system parameters, under the specific conditions of $P_w=1.0\text{p.u.}$, $T_j=5.7\text{s}$, and a fault duration of 0.15s, it can be calculated that the stable equilibrium point $\delta_s=0.1\text{rad}$, the unstable equilibrium point $\delta_u=2.06\text{rad}$, and the fault clearing angle $\delta_c=0.72\text{rad}$, as shown in Figure 5. The accelerating area of the SC equals the decelerating area, i.e., $S_1=S_2=0.62$, and the SC is in a critical stable state. At this moment, the active power delivery of renewable energy units is the maximum value. When P_w increases further, the fault clearing angle will also increase accordingly, the accelerating area S_1 will exceed the maximum decelerating area $S_{2\max}$, and the SC's transient power-angle instability will occur. The maximum active power delivery of renewable energy sources when the SC is in critical stability can be derived from $S_1=S_{2\max}$. If the active power delivery of renewable energy units during pre-fault steady-state operation is greater than this maximum value, it will cause acceleration of the SC's rotor and increase the risk of its transient power-angle instability.

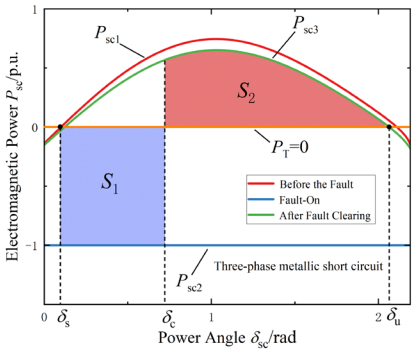

Figure 5. Equal Area Criterion (Critical Stability) for the simplified renewable energy power transmission configuration integrated with SC at $P_w=1.0\text{p.u.}$

4. The influence mechanism of the active power output of renewable energy sources on the transient power-angle stability of SC

4.1. Transient performance characteristics of SC after the fault clearance

Given the rated capacity of the SC and with $Q_w=0$, the correlation curve between the PCC voltage amplitude and the power angle of the SC can be plotted according to the analytical expression of U_b' as shown in Figure 6. A further analysis is conducted on the changes of PCC voltage amplitude following the clearance of the fault. Since the relative power angle of the SC with respect to the receiving-end system continues to increase after fault clearing, the PCC voltage amplitude gradually decreases, failing to recover to above 0.9p.u.. quickly after fault clearing. At the same power angle, the PCC voltage amplitude shows a more obvious downward trend with the growth of the active power output of renewable energy sources. In addition, the larger the P_w, the lower the valley value of the voltage curve, indicating that the growth in active power output from renewable energy sources will aggravate the voltage sag at the PCC during the transient process after a fault.

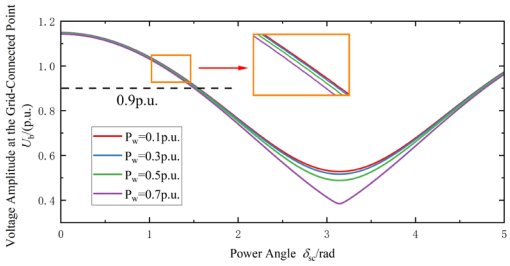

Figure 6. Profiles of PCC voltage amplitude corresponding to various active power output levels of renewable energy sources subsequent to fault clearing

Still using the aforementioned system parameters, the SC's power-angle characteristic curves under different active power outputs of renewable energy sources after fault clearance can be plotted based on the functional relationship of $P_{sc3}-\delta_{sc}$ in Equation (14), as shown in Figure 7.

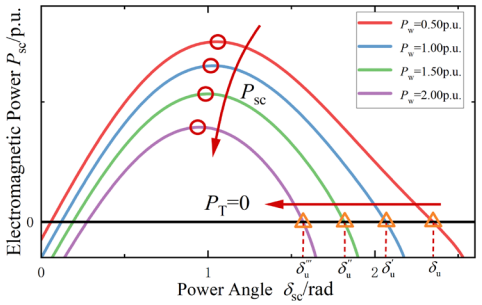

Figure 7. Power-angle profile curves of the SC corresponding to various active power output levels of renewable energy sources subsequent to fault clearing

As observed in Figure 7, assuming the mechanical power input P_T to the SC is zero, with the growth of the active power output of renewable energy sources, the unstable equilibrium point of the SC shifts to the left after fault clearing, the power limit point gradually decreases, and the power-angle characteristic curve shows an overall downward shift trend. This indicates that the maximum decelerating area decreases after fault clearance, which is not conducive to the transient power-angle stability of SC and increases the risk of its transient instability.

4.2. The influence mechanism of the active power output of renewable energy sources on stability indices based on the trajectory analysis method

To quantitatively assess how variations in active power output from renewable energy sources affect the SC's transient power-angle stability, the trajectory analysis method is introduced into the quantitative analysis of the SC's transient process. By constructing a correlation model between stability indices and the active power delivery of renewable energy sources, the sensitivity characteristics of stability indices to changes in active power output are analyzed, and the direction and extent of the impact of different active power outputs of renewable energy sources on the SC's transient stability are clarified. This provides mechanistic support for the subsequent quantitative characterization of the SC's transient stability through simulation verification.

The trajectory analysis method is based on the single-machine energy function and is used to evaluate the stability of power systems. This method simulates the dynamic response of the SC after a fault through numerical simulation, extracts the SC's operating trajectory data (such as accelerating power $P_a(t)$ and rotational speed $\omega_{sc}(t)$), analyzes the trajectory data based on the single-machine energy function, and calculates indices reflecting its stability.

Through Equation (1), the single-machine energy function can be constructed as follows:

$$V_{sc} = V_{KEsc}(\omega_{sc}) + V_{PEsc}(\delta_{sc}) \tag{18}$$

Among them,

$$\begin{aligned} V_{KEsc}(\omega_{sc}) &= \frac{1}{2} M_{sc} \omega_{sc}^{\ 2}(t) \\ V_{PEsc}(\delta_{sc}) &= \int_{\delta_c}^{\delta_{sc}} [-P_a(u)] du \\ V_{PEsc}(t) &= \int_{t_c}^{t} \omega_0 [-P_a(u)] \omega_{sc}(u) du \end{aligned} \tag{19}$$

In the above equation, V_{sc} is the transient energy of the SC with $\dot{V}_{sc} = 0$; $V_{KEsc}(\omega_{sc})$ is the transient kinetic energy of the SC; $V_{PEsc}(\delta_{sc})$ and $V_{PEsc}(t)$ are the transient potential energies of the SC, t_c is the fault clearing time, and δ_c is the fault clearing angle corresponding to the time t_c.

Since the accelerating power of the SC equals $P_a = P_T - P_{sc} = -P_{sc}$, the transient potential energy of the SC can be further simplified as follows:

$$V_{PEsc}(\delta_{sc}) = \int_{\delta_c}^{\delta_{sc}} P_{sc3}(u) du \tag{20}$$

Combined with Equation (14), the formula for the transient potential energy is given below:

$$V_{PEsc}(\delta_{sc}) = \int_{\delta_c}^{\delta_{sc}} \frac{E'}{X_{sc}} \cdot \frac{U_b'^2 \cdot \left[2U_b'^2 \cdot \frac{E_s X_1' \sin\delta_{sc}}{X_L'} - P_w X_1' \left(\frac{E' X_1'}{X_{sc}} + \frac{E_s X_1' \cos\delta_{sc}}{X_L'} \right) \right]}{4U_b'^4 + P_w^{\ 2} X'^2} d\delta_{sc} \tag{21}$$

It can be seen from Figure 5 that when $P_{sc} > 0$, the SC is in the phase of injecting active power into the system. The integrand of Equation (21) is positive, so the integral V_{PEsc} monotonically increases with the increase of δ_{sc}, and the transient potential energy of the SC accumulates. Meanwhile, P_{sc} shifts downward with the increase of P_w in Figure 7, and the rate of integral growth gradually slows down. This is manifested as the slope of the V_{PEsc} curve decreases with the increase of δ_{sc} as P_w increases. After the SC completely releases the kinetic energy accumulated during the fault, if the transient potential energy does not reach or exceed the critical maximum potential energy, the transient state remains stable. When P_{sc} changes from positive to negative, the transient potential energy of the SC starts to release, and the SC switches to the phase of absorbing active power from the system. The integrand becomes negative, and V_{PEsc} monotonically decreases with the increase of δ_{sc} at this time. As the absolute value of P_{sc} increases with the increase of P_w, the rate of decrease of V_{PEsc} gradually accelerates, that is, the absolute value of the curve's slope increases with the increase of δ_{sc} as P_w increases.

Based on Equation (21), the transient potential energy-power angle curves under different active power outputs of renewable energy sources are plotted as shown in Figure 8. As shown in Figure 7, with the active power output of renewable energy during steady-state operation gradually increasing, the electromagnetic power curve P_{sc3} of the SC shifts downward, and the power limit point of the SC decreases. This reduces the electromagnetic power P_{sc3} of the SC at the same power angle, leading to insufficient braking power required for rotor deceleration and weakened deceleration capability. Consequently, the maximum deceleration area S_{2max} decreases with the increase of P_w, and the maximum potential energy V_{PEmax} that can be accumulated during the transient process

gradually decreases, which is manifested as a leftward shift of the curve peak and a decrease in its value.

This indicates that the transient stability margin of the synchronous condenser gradually decreases as the active power output of renewable energy increases.

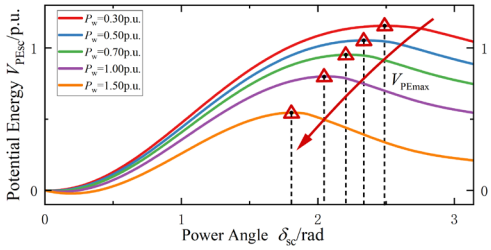

Figure 8. Transient potential energy-power angle curves of the system under different active power output levels of renewable energy sources

If the potential energy of the SC increases monotonically from its minimum value to its maximum value after the fault, and there is at most one point in this time interval where $dP_a(t)/dt = 0$, the trajectory of the SC is defined as a canonical trajectory. If the potential energy of the SC increases non-monotonically from its minimum value to its maximum value after the fault, and there exist multiple points in this time interval where $dP_a(t)/dt = 0$, the trajectory of the SC is defined as a non-canonical trajectory. Regardless of whether the trajectory is canonical or non-canonical, t_a is defined as the time corresponding to the minimum potential energy within the selected time interval, and t_b is defined as the time corresponding to the maximum potential energy. At time t_b, the stability index of the SC is given by:

$$S = \frac{\frac{dV_{PEsc}}{d\delta_{sc}}|t_b}{V_{PEsc}(t_b,t_a)} = \frac{-P_a(t_b)}{V_{PEsc}(t_b,t_a)} \frac{P_{sc3}(t_b)}{\int_{t_a}^{t_b} \omega_0 \cdot P_{sc3}(u) \cdot \omega_{sc}(u) du} \quad (22)$$

Combined with Equations (14), (21), and (22), the detailed expression of the stability index of the SC is provided in with the detailed expression provided in Equation (22) in Appendix A.

To explicitly characterize the responsive sensitivity of the stability index to renewable energy active power output, sensitivity analysis $\partial S/\partial P_w$ is employed:

$$\frac{\partial S}{\partial P_w} = \frac{\frac{\partial P_{sc3}(t_b)}{\partial P_w} \cdot V_{PEsc}(t_b,t_a) - \frac{\partial V_{PEsc}(t_b,t_a)}{\partial P_w} \cdot P_{sc3}(t_b)}{V_{PEsc}(t_b,t_a)^2} \quad (23)$$

Through mathematical derivation, $\partial P_{sc3}(t_b)/\partial P_w < 0$, with the detailed derivation process provided in with the detailed expression provided in Equation (25-30) in Appendix A. The potential energy variation $V_{PEsc}(t_b,t_a)$ from t_a to t_b is greater than 0. When the potential energy achieves its maximum value at time t_b: if it does not reach the critical maximum potential energy, then $P_{sc3}(t_b) > 0$. According to the equal-area criterion in Figure 4, a rise in the active power output P_w of renewable energy sources causes the SC's power-angle characteristic curve P_{sc2} during the fault to decrease. Without changing the stable equilibrium point or the fault duration, the fault clearing angle δ_c remains unchanged. At this time, the accelerating area increases, the kinetic energy accumulated in the rotor rises, and the potential energy variation after fault clearing also increases, i.e., $\partial V_{PEsc}(t_b,t_a)/\partial P_w > 0$, thus $\partial S/\partial P_w < 0$. If the potential energy exactly reaches the critical maximum potential energy when peaking, then $P_{sc3}(t_b) = 0$, leading to $\partial S/\partial P_w < 0$. If the potential energy exceeds the critical maximum potential energy when peaking, the power angle swings past the unstable equilibrium point δ_u, resulting in $P_{sc3}(t_b) < 0$. The potential energy variation $V_{PEsc}(t_b,t_a)$ equals the critical maximum potential energy, while the magnitude of P_{sc3} shifts downward with the increase of P_w. This means the critical maximum potential energy decreases as P_w rises, with $\partial V_{PEsc}(t_b,t_a)/\partial P_w < 0$, thus $\partial S/\partial P_w < 0$. From the above analysis, under the scenario of a three-phase metallic short-circuit fault, the stability index characterizing the SC's transient stability margin decreases as the active power output level of renewable energy systems increases, and the transient power-angle stability gradually deteriorates. When the stability index approaches zero, the SC loses transient power-angle stability.

5. Example Analysis

To verify the mechanism of the SC transient characteristics under faults derived from the analytical expressions in this paper, as well as how changes in renewable energy active power delivery affect the voltage at the PCC and the SC's transient power-angle stability, a simplified renewable energy transmission system model as shown in Figure 1(a) is built in the Power System Analysis Software Package (PSASP) for simulation. The renewable energy source adopts a doubly-fed induction wind turbine with a rated capacity of 500MVA. To better align with engineering practice, realize a weak disturbance scenario, and ensure the steady-state active power output of renewable energy, the fault is configured as a three-phase solid short-circuit fault occurring at the remote end of the system, where the fault starts at 0.5s and lasts for 0.15s. Key parameters used in the simulation are listed in Table 1.

Table 1. Main simulation parameters of the simplified renewable energy transmission system

Simulation parameters	Numerical settings
Base capacity S_n	100MVA
Capacity of the SC S_{sc}	100MVA
E'	1.2
T_j	5.569s
X'_d	0.1163
X_T	0.143
X_L	0.260
E_s	1.0

5.1. Verification of the Mechanism of SC Transient Characteristics

As can be observed from Figure 9, the parameter P_w is configured at 1.0p.u. for steady-state operation prior to the fault occurrence. The active power output of renewable energy sources exhibits slight fluctuations at the fault occurrence time of 0.5s but remains basically around 1.0p.u. during the entire fault period. After fault clearing, the P_w returns to the steady-state level. The SC generates negative electromagnetic power during the fault period and maintains it basically near -1.0p.u., indicating that the SC continuously absorbs the active power generated by renewable energy sources during the fault period. The amount of absorbed active power is approximately equal to the mean magnitude of the overall active power output of renewable energy sources during the fault period, i.e., 1.0p.u., which is consistent with the analysis result in the mechanism study that the amount of active power absorbed by the SC during the fault period equals the active power delivery of renewable energy sources. In addition, the SC's power angle continues to swing positively after fault clearing. Under the condition of $P_w = 1.0$p.u., the power angle presents damped oscillations, indicating that the SC maintains transient power-angle stability.

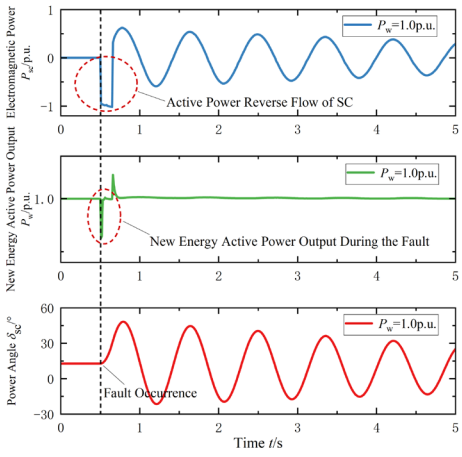

Figure 9. Time-domain simulation waveforms of P_{sc}, δ_{sc} of the SC and active power output P_w of renewable energy sources at $P_w = 1.0$p.u.

Three different operating conditions are set, namely $P_w = 1.0$p.u., $P_w = 1.5$p.u. and $P_w = 2.0$p.u., to analyze the voltage fluctuation at the PCC with the increase of P_w. As is illustrated in Figure 10(a), during the fault period, the severity of transient under-voltage deepens continuously with the increase of P_w. After fault clearing, voltage drop also occurs at the PCC. With the increase of P_w, the voltage drop at the PCC lasts longer and becomes more severe, which poses a negative impact on maintaining the PCC voltage stability after the fault. In Figure 10(b), the power angle continues to swing positively after fault clearing, and the voltage at the PCC decreases gradually with the increase of the power angle. Essentially, the post-fault voltage sag phenomenon at the PCC shown in Figure 10(a) is caused by the increased swing amplitude of the power angle with the rise of P_w, which in turn results in a larger power angle value after fault clearing.

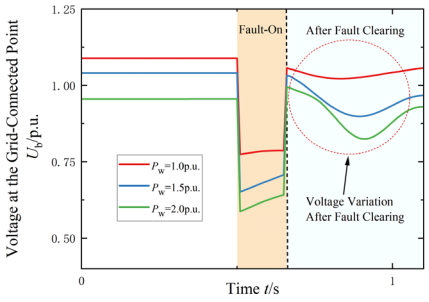

(a) Voltage fluctuation curves at the PCC under various P_w conditions

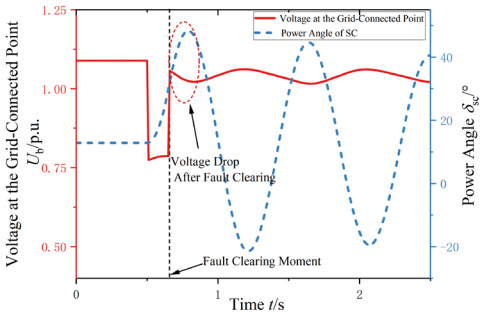

(b) Voltage at the PCC versus SC power angle curve

Figure 10. Voltage waveforms at the PCC

5.2. Verification of the impact of renewable energy active power output on stability index

The trajectory analysis method is an important approach for evaluating the transient stability of synchronous machines. To verify how changes in renewable energy active power output affect the stability index of the SC, simulation values of transient parameters such as angular velocity and accelerating power of the SC under different P_w conditions are obtained through simulation, and then the stability index S characterizing the SC's transient stability status is derived.

The active power output of renewable energy is sequentially set to 0.50p.u., 0.75p.u., 1.00p.u., 1.50p.u. and 1.80p.u., and the relevant simulation results are presented as follows.

Table 2. Simulation results of SC transient parameters under different P_w conditions

Active power output of renewable energy sources P_w / p.u.	Power angle $\delta_{sc}(t_b)$/°	Potential energy variation $V_{PEsc}(t_b,t_a)$ /p.u.	Accelerating power $P_a(t_b)$/ p.u.	Time t_b / s
0.5	18.5284	0.0181	-0.2318	0.79
0.75	32.9154	0.0635	-0.4257	0.79
1.00	48.3086	0.1390	-0.6167	0.79
1.5	-49.3637	0.1575	0.0507	1.03
1.8	-58.8954	0.2171	0.0059	1.04

Based on the simulation results in Table 2, during the process of maintaining transient stability, the negative value of the accelerating power of the SC increases with the rise of P_w, which increases the accumulation rate of the transient energy of the SC rotor and essentially accelerates the rate of the SC potential energy variation. However, during the process of transient instability, the reduction amplitude of the accelerating power is relatively small, and with the continuous deterioration of transient stability, the absolute value of the accelerating power approaches zero. With the increase of P_w, the total energy accumulated by the SC eventually undergoes a fundamental change. The swing amplitude of the power angle becomes larger when the potential energy achieves the peak magnitude, indicating that the security margin of the SC for maintaining transient stability attenuates at an accelerated pace.

It can be seen from Figure 11 that as P_w increases from 0.50p.u. to 1.80p.u., the potential energy variation under the five operating conditions increases continuously. In Figure 11(a), the SC maintains transient stability, and the system potential energy exhibits a variation pattern of initial increase followed by subsequent decrease after fault clearing. At 0.65s, the initial minimum value of the potential energy is reached, and then keeps rising to hit the first maximum value at 0.79s. With the same increment of P_w, The time t_a corresponding to the first occurrence of the potential energy's minimum value and the time t_b corresponding to the initial emergence of its maximum value keep unchanged under the three operating conditions. With the increase in the negative value of accelerating power, the variation rate of potential energy becomes faster, thus leading to the increase in potential energy variation. In Figure 11(b), the SC is in critical stability when $P_w = 1.50$p.u.. As the P_w increases to 1.80p.u., the SC loses transient stability, the potential energy variation increases, and the time when the potential energy achieves its peak is delayed, with t_b changing from 1.03s to 1.04s and the peak value also increasing to a certain extent. However, the accelerating power at time t_b changes slightly. The increase in potential energy variation and the accelerating power continuously approaching zero cause the stability index to gradually decrease to near zero during the transient instability process.

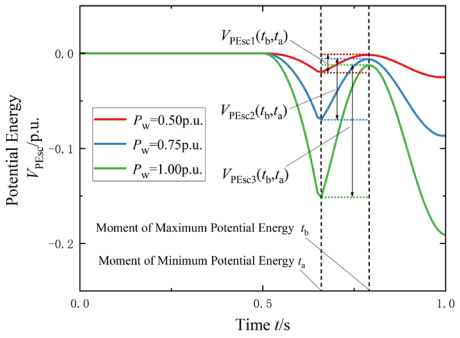

(a) Transient power angle stability

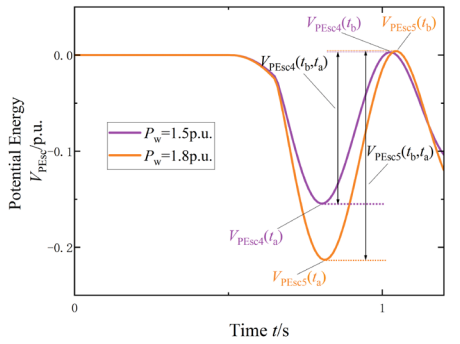

(b) Transient power angle instability

Figure 11. Different P_w conditions: potential energy-time variation curves

The variation of the SC rotor speed is shown in Figure 12. As is demonstrated in Figure 12(a), during the fault period, the SC rotor speed increases positively, and with the rise of P_w, the speed variation rate becomes faster, such that the extent to which the speed exceeds the synchronous speed is greater when the fault is eliminated. After fault clearing, the SC's active power gradually rises, and the rotor speed starts to decrease gradually. The

increase in the P_w leads to a larger negative value of the accelerating power, resulting in a deeper drop and a faster decrease rate of the rotor speed. In Figure 12(b), after the fault occurs, the SC rotor speed is lower than the synchronous speed and begins to increase negatively. After fault clearing, the rotor speed still swings in the negative direction, and with the increase of P_w, the negative speed variation rate becomes larger. Under the operating conditions of $P_w = 1.50$p.u. and $P_w = 1.80$p.u., since the rotor speed remains lower than the synchronous speed after the fault occurs, $d\delta_{sc}/dt < 0$ and the power angle swings in the negative direction first.

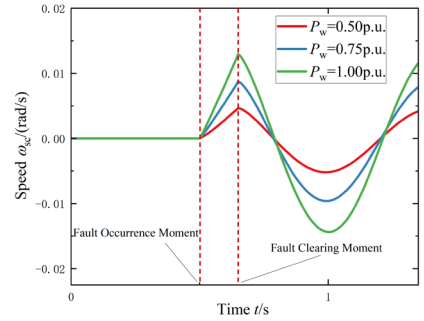

(a) Transient power angle stability

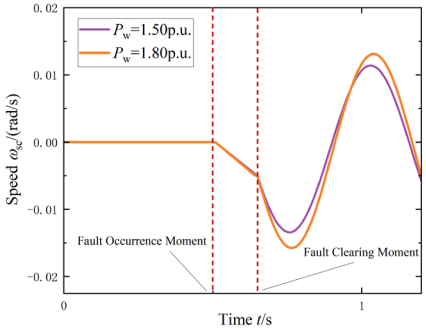

(b) Transient power angle instability

Figure 12. Different P_w conditions: rotor speed-time variation curves

Table 3 lists the stability indices of the SC, and its power angle dynamic response characteristic curves are shown in Figure 13. As P_w increases, the swing amplitude of the SC's power angle expands continuously, and the peak value of the power angle becomes larger. Meanwhile, the absolute value of the stability index S gradually decreases. When transient instability occurs, the stability index drops close to zero, which verifies the impact of P_w variations on the stability index as analyzed in the mechanism study. Under the first three operating conditions, after fault clearing, the rotor speed remains higher than the synchronous speed due to the accumulated rotor kinetic energy, so the power angle continues to increase and reaches the first maximum value at 0.79 s. Moreover, the power angle's peak time corresponds to the maximum of the system potential energy curve. The power angle shows damped oscillations as a whole, indicating that the SC maintains transient power angle stability. Under the latter two operating conditions, the rotor speed is lower than the synchronous speed first after the fault, so the power angle swings in the negative direction initially. Subsequently, as the rotor speed diverges continuously in the negative direction, the extent to which the speed is lower than the synchronous speed deepens gradually, leading to the overall negative oscillation of the power angle and the occurrence of transient power angle instability. Variations in the active power output of renewable energy sources change the power balance state of the SC, directly affect the accelerating power, induce the dynamic adjustment of its rotor speed, and ultimately result in different swing amplitudes of the SC power angle. The stability indices in Table 3 match well with the power angle response curves in Figure 13, which accurately reflect the transient power angle stability status of the SC.

Table 3. Stability indices of the SC under different P_w conditions

Active power output of renewable energy sources P_w / p.u.	Stability index
0.5	12.7897
0.75	6.7062
1.00	4.4384
1.5	-0.3221
1.8	-0.0269

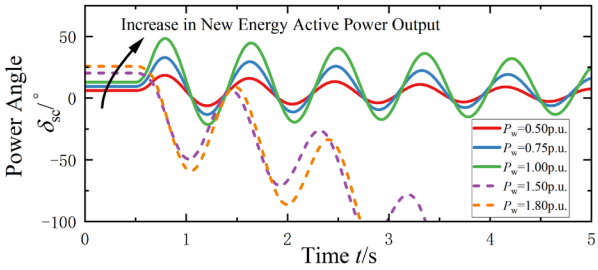

Figure 13. Power angle-time curves of the SC under different P_w conditions

6. Conclusions

In this paper, a simplified renewable energy transmission system model is established. Based on certain assumptions, the analytical expressions of the SC electromagnetic power accounting for the impact of different renewable energy active power outputs before, during and after faults are derived through system

equivalence. The power transmission relationship between the SC and renewable energy sources during faults is analyzed based on the equal-area criterion, revealing the internal mechanism causing the transient instability of the SC. Combined with the trajectory analysis method, the influence mechanism of renewable energy active power output variations on the stability index is analyzed using the post-fault power angle characteristics, and the key conclusions below are summarized:

(i) During faults, the SC reversely absorbs the active power output from renewable energy sources, causing its rotor to accelerate during the fault period and thus leading to its transient instability. After fault clearing, the voltage sag at the PCC is essentially caused by the continuous increase of the power angle after the fault. Moreover, as the active power output of renewable energy sources rises, the continuous positive swing of the power angle exacerbates the degree of voltage sag at the PCC.

(ii) The rise of renewable energy active power output affects the unbalanced power of SC, which in turn causes changes in the rotor speed and an increase in potential energy variation, resulting in a larger swing amplitude of the power angle. The stability index characterizing the transient stability of the SC gradually decreases, and approaches zero when transient instability occurs.

Finally, verification studies are carried out through simulation experiments, and the results demonstrate the reliability of the theoretical analysis. The research in this paper is based on certain assumptions, without considering the effect of the LVRT dynamic characteristics of renewable energy sources on the theoretical analysis. In future research, the transient stability of the SC can be further investigated by combining the specific control strategies of renewable energy sources during the transient process.

Appendix A.

Expressions of $\sin\delta_b$ and $\cos\delta_b$ in Equation (7):

$$\begin{cases} \sin\delta_b = \dfrac{U_b\cdot\left[P_wX_I\left(\dfrac{E'X_I\cos\delta_{sc}}{X_{sc}}+\dfrac{E_sX_I}{X_L}\right)+(2U_b^{\ 2}-Q_wX_I)\dfrac{E'X_I\sin\delta_{sc}}{X_{sc}}\right]}{(2U_b^{\ 2}-Q_wX_I)^2+(P_wX_I)^2} \\ \cos\delta_b = \dfrac{U_b\cdot\left[(2U_b^{\ 2}-Q_wX_I)\left(\dfrac{E'X_I\cos\delta_{sc}}{X_{sc}}+\dfrac{E_sX_I}{X_L}\right)-P_wX_I\dfrac{E'X_I\sin\delta_{sc}}{X_{sc}}\right]}{(2U_b^{\ 2}-Q_wX_I)^2+(P_wX_I)^2} \end{cases} \quad (7)$$

Detailed expression of U_b in Equation (9):

$$U_b=\sqrt{\frac{4Q_wX_I+\frac{E'^2X_I^2}{X_{sc}^2}+\frac{2E'E_sX_I^2\cos\delta_{sc}}{X_{sc}X_L}+\frac{E_s^2X_I^2}{X_L^2}+\sqrt{\left(4Q_wX_I+\frac{E'^2X_I^2}{X_{sc}^2}+\frac{2E'E_sX_I^2\cos\delta_{sc}}{X_{sc}X_L}+\frac{E_s^2X_I^2}{X_L^2}\right)^2-16\left(P_w^2X_I^2+Q_w^2X_I^2\right)}}{8}} \quad (9)$$

Detailed expression of U_b':

$$U_b'=\sqrt{\frac{4Q_wX_I'+\frac{E'^2X_I'^2}{X_{sc}^2}+\frac{2E'E_sX_I'^2\cos\delta_{sc}}{X_{sc}X_L'}+\frac{E_s^2X_I'^2}{X_L'^2}+\sqrt{\left(4Q_wX_I'+\frac{E'^2X_I'^2}{X_{sc}^2}+\frac{2E'E_sX_I'^2\cos\delta_{sc}}{X_{sc}X_L'}+\frac{E_s^2X_I'^2}{X_L'^2}\right)^2-16\left(P_w^2X_I'^2+Q_w^2X_I'^2\right)}}{8}} \quad (24)$$

Detailed expression of the stability index in Equation (22):

$$S=\frac{P_{sc3}(t_b)}{V_{PEsc}(t_b,t_a)}=\frac{\dfrac{E'}{X_{sc}}\cdot\dfrac{U_b'^2\cdot\left[2U_b'^2\cdot\dfrac{E_sX_I'\sin\delta_{sc}(t_b)}{X_L'}-P_wX_I'\left(\dfrac{E'X_I'}{X_{sc}}+\dfrac{E_sX_I'\cos\delta_{sc}(t_b)}{X_L'}\right)\right]}{4U_b'^4+P_w^{\ 2}X'^2}}{\int_{t_a}^{t_b}\omega_b\cdot\dfrac{E'}{X_{sc}}\cdot\dfrac{U_b'^2\cdot\left[2U_b'^2\cdot\dfrac{E_sX_I'\sin\delta_{sc}(u)}{X_L'}-P_wX_I'\left(\dfrac{E'X_I'}{X_{sc}}+\dfrac{E_sX_I'\cos\delta_{sc}(u)}{X_L'}\right)\right]}{4U_b'^4+P_w^{\ 2}X_I'^2}\cdot\omega_{sc}(u)du} \quad (22)$$

The following is the derivation process for $\partial P_{sc3}(t_b)/\partial P_w$:

From Equation (14): $P_{sc3}(t_b)=\dfrac{E'}{X_{sc}}\cdot\dfrac{N}{D}$

Where, $N=U_b'^2\cdot\left[2U_b'^2\cdot\dfrac{E_sX_I'\sin\delta_{sc}(t_b)}{X_L'}-P_wX_I'\left(\dfrac{E'X_I'}{X_{sc}}+\dfrac{E_sX_I'\cos\delta_{sc}(t_b)}{X_L'}\right)\right]$

, $D=4U_b'^4+P_w^{\ 2}X_I'^2$.

Then, $\dfrac{\partial P_{sc3}(t_b)}{\partial P_w}=\dfrac{E'}{X_{sc}}\cdot\dfrac{\dfrac{\partial N}{\partial P_w}\cdot D-N\cdot\dfrac{\partial D}{\partial P_w}}{D^2}$.

$$\begin{aligned}\frac{\partial N}{\partial P_w}=&\frac{\partial U_b'^2}{\partial P_w}\cdot\left[2U_b'^2\cdot\frac{E_sX_I'sin\delta_{sc}(t_b)}{X_L'}-P_wX_I'\left(\frac{E'X_I'}{X_{sc}}+\frac{E_sX_I'cos\delta_{sc}(t_b)}{X_L'}\right)\right]\\&+U_b'^2\cdot\left[2\frac{\partial U_b'^2}{\partial P_w}\cdot\frac{E_sX_I'sin\delta_{sc}(t_b)}{X_L'}-X_I'\left(\frac{E'X_I'}{X_{sc}}+\frac{E_sX_I'cos\delta_{sc}(t_b)}{X_L'}\right)\right]\end{aligned} \quad (25)$$

$$\frac{\partial D}{\partial P_w}=8U_b'^2\frac{\partial U_b'^2}{\partial P_w}+2P_wX_I'^2 \quad (26)$$

From Equation (24) , when $Q_w=0$, the expression of $U_b'^2$ is as follows:

$$U_b'^2=\frac{E'+\sqrt{E'^2-16F'}}{8} \quad (27)$$

Where, $E'=\dfrac{E'^2X_I'^2}{X_{sc}^{\ 2}}+\dfrac{2E'E_sX_I'^2\cos\delta_{sc}(t_b)}{X_{sc}X_L'}+\dfrac{E_s^{\ 2}X_I'^2}{X_L'^2}$,

$F'=P_w^{\ 2}X_I'^2$.

$$\frac{\partial U_b'^2}{\partial P_w}=\frac{-2P_wX_I'^2}{\sqrt{E'^2-16F'}} \quad (28)$$

Substituting Equation (28) into Equations (25) and (26) yields:

$$\frac{\partial N}{\partial P_w}=\frac{-8P_wU_b'^2X_I'^2}{\sqrt{E'^2-16F'}}\cdot\frac{E_sX_I'\sin\delta_{sc}(t_b)}{X_L'}-X_I'U_b'^2\left(\frac{E'X_I'}{X_{sc}}+\frac{E_sX_I'\cos\delta_{sc}(t_b)}{X_L'}\right) \quad (29)$$

$$\frac{\partial D}{\partial P_w}=\frac{-2E'}{\sqrt{E'^2-16F'}}\cdot P_wX_I'^2 \quad (30)$$

It can be obtained from the above equation that $\partial D/\partial P_w<0$. Assuming that the power angle $\delta_{sc}(t_b)$ at which the potential energy achieves the maximum value does not exceed π/2, it follows that $\partial N/\partial P_w<0$. In addition, $D=4U_b'^4+P_w^{\ 2}X_I'^2>0$. After fault clearing, a certain degree of voltage sag occurs at the PCC, resulting in a small value of $U_b'^4$ that is close to 0; thus, $N=-U_b'^2P_wX_I'\left(E'X_I'/X_{sc}+E_sX_I'\cos\delta_{sc}(t_b)/X_L'\right)$ is less than zero. In summary, it can be concluded that $\partial P_{sc3}(t_b)/\partial P_w<0$.

Acknowledgements

This research was financially supported by CGN (Xing'an League) New Energy Co., Ltd. through the research project "Research on Transient Stability Modeling, Simulation Analysis and Verification of Large-Scale Wind Farms with Distributed Synchronous Condensers", and we express our sincere gratitude for this support.

References

[1] Zhang Z G, Kang C Q. Challenges and Prospects for Constructing the New-Type Power System Towards a Carbon Neutrality Future. Proceedings of the CSEE, 2022, 42(08): 2806-2819. (In Chinese)

[2] National Energy Administration. National Energy Administration Releases National Power Industry Statistical Data for January-July 2025. (2025-08-23) [2025-09-26]. https://www.nea.gov.cn/20250823/7e111f0a60ac44438346bd8332db345e/c.html. (In Chinese)

[3] Study on China's Energy and Power Development Plan for 2030 and Outlook for 2060. Global Energy Interconnection Development and Cooperation Organization, 2021. (In Chinese)

[4] Liu X Y, Xin H H, Zheng D, Cao B. Temporary overvoltage assessment and suppression in heterogeneous renewable energy power systems. International Journal of Electrical Power & Energy Systems, 2024, 155: 109472.

[5] Li W, Qian Z W, Wang Q, Wang Y, Liu F, Zhu L. Transient Voltage Control of Sending-End Wind Farm Using a Synchronous Condenser Under Commutation Failure of HVDC Transmission System. IEEE Access, 2021, 9: 54900-54911.

[6] Wen Y F, Yang Y H, Xing P X. Review on Evaluation Methods of New Energy Accommodation Capacity Under Multi-dimensional Constraints. Proceedings of the CSEE, 2024, 44(01): 127-147. (In Chinese)

[7] Guo Q, Li Z Q. Summarization of synchronous condenser development. Proceedings of the CSEE, 2023, 43(15): 6050-6064. (In Chinese)

[8] Hadavi S, Saunderson J, Mehrizi-Sani A, Bahrani B. A planning method for synchronous condensers in weak grids using semi-definite optimization. IEEE Transactions on Power Systems, 2022, 38(2): 1632-1641.

[9] Igbinovia F O, Fandi G, Müller Z, Svec J, Tlustý J. Optimal location of the synchronous condenser in electric-power system networks. 2016 17th International Scientific Conference on Electric Power Engineering (EPE). IEEE, 2016: 1-6.

[10] Wang T, Pei L, Wang J M, Wang Z P. Overvoltage suppression under commutation failure based on improved voltage-dependent current order limiter control strategy. IEEE Transactions on Industry Applications, 2022, 58(4): 4914-4922.

[11] Hadavi S, Mansour M Z, Bahrani B. Optimal Allocation and Sizing of Synchronous Condensers in Weak Grids With Increased Penetration of Wind and Solar Farms. IEEE Journal on Emerging and Selected Topics in Circuits and Systems, 2021, 11(1): 199-209.

[12] Kundur P, Balu N J, Lauby M G. Power System Stability and Control. McGraw-Hill: New York, USA, 1994: 625–701.

[13] Shen G J, Xin H H, Liu X Y, Tu J Z, Wang K. Analysis on Synchronous Instability Mechanism and Influencing Factors of Synchronous Condensers in Large-Scale New Energy Bases. Automation of Electric Power Systems, 2022, 46(20): 100-108. (In Chinese)

[14] Li B F, Yang S H, Hu Y W, Hao Z G, Zhao T Q. Rotor Angle Transient First-Swing Stability Analysis of Synchronous Condensers Near Wind Farms. 2023 IEEE Power & Energy Society General Meeting (PESGM). IEEE, 2023: 1-5.

[15] Wang T, W X T, Han Z C, Wang Z P, Zhao W. Analysis on Transient Characteristics and Research on Transient Power Angle Stability Mechanism of Distributed Synchronous Condensers. Transactions of China Electrotechnical Society, 2025, 40(01): 36-51. (In Chinese)

[16] Wang X T, W T, Han Z C, Wang Z P, Lv Z. Mechanism of LVRT Control of IBR on Transient Stability of Synchronous Condenser. 2025 IEEE Power & Energy Society General Meeting (PESGM). IEEE, 2025: 1-5.

[17] Liu X Y, Xin H H, Zheng D, Chen D, Tu J Z. Transient Stability of Synchronous Condenser Co-Located With Renewable Power Plants. IEEE Transactions on Power Systems, 2023, 39(1): 2030-2041.

[18] Liu X Y, Xin H H, Shan Y P, Zheng D, Chen D. Transient Stability of Synchronous Condenser Co-Located With Renewable Power Plants Under High-Resistance Faults and Risk Mitigation. IEEE Transactions on Sustainable Energy, 2024, 15(4): 2581-2593.

[19] Zhao T Q, Li B F, Yang S H, Xie H, Zhang J. Analysis on Influencing Factors of Transient Power Angle Stability of Distributed Synchronous Condensers in New Energy Plants. Automation of Electric Power Systems, 2023, 47(16): 114-122. (In Chinese)

[20] Gu Y X, Zhou Y B. Analysis on the Influence of the Active Power Recovery Rate on the Transient Stability Margin of a New Power System. Processes, 2025, 13(7): 2020.

[21] Pei J X, Yao J, Liu R K, Zeng D Y, Sun P, Zhang H L. Characteristic Analysis and Risk Assessment for Voltage–Frequency Coupled Transient Instability of Large-Scale Grid-Connected Renewable Energy Plants During LVRT. IEEE Transactions on Industrial Electronics, 2019, 67(7): 5515-5530.